

# Room-temperature plasticity in Ag<sub>2</sub>Te induced by Ag ions hopping

Received: 24 August 2025

Accepted: 28 January 2026

Published online: 05 February 2026

 Check for updates

Anan Guo<sup>1,2,4</sup>, Keke Liu<sup>1,4</sup>, Zhengzhou Wang<sup>1,2</sup>, Lingxiao Yu<sup>1</sup>, Yongqiang Li<sup>1</sup>, Lin Liao<sup>1,2</sup>, Dongwang Yang<sup>1</sup>, Xianli Su<sup>1</sup>, Xiahan Sang<sup>1</sup>, Xinfeng Tang<sup>1</sup>, Qingjie Zhang<sup>1</sup> & Jinsong Wu<sup>1,2,3</sup> ✉

The discovery of silver chalcogenides ductile semiconductors with high room-temperature plasticity holds significant promise for the development of bendable thermoelectric and electronic devices. However, the atomic-scale origins of their plasticity, ranging from dislocation slip to sublattice amorphization, remain diverse and material-specific. Here, we report a distinct deformation mechanism in Ag<sub>2</sub>Te through stress-driven and ionic-hop-mediated domain rotation. By in-situ scanning/transmission electron microscopy (S/TEM), we directly observe the hopping of Ag ions to adjacent vacancies stabilizes the deformed Te-sublattice and facilitates a coordinated  $\sim 92.2^\circ$  lattice rotation that accommodates substantial plastic strain. This mechanism, which preserves long-range crystallinity, contrasts with both traditional dislocation-mediated plasticity and stress-induced amorphization pathways. Combined with its excellent thermoelectric performance (ZT value of  $\sim 0.67$ ) at room temperature, Ag<sub>2</sub>Te emerges as a promising flexible electronic material.

Flexible semiconductors have received a lot of attention due to their potential in the development of bendable, stretchable and wearable electronic devices, such as thermoelectric generators and flexible transistors<sup>1–9</sup>. Notably, several inorganic semiconductors, primarily chalcogenides, have been discovered to exhibit significant room-temperature plasticity<sup>1,10–24</sup>. This unique property enables the direct integration of robust electronic components into flexible systems, bypassing the need for complex film-on-substrate architectures<sup>25–31</sup>.

Despite these promising prospects, the atomic mechanisms responsible for large plastic deformation in these inherently brittle materials are diverse and not fully unified. Early studies often attributed plasticity to dislocation motion and stacking faults<sup>17,32–45</sup>. More recent work on silver chalcogenides has revealed alternative pathways; for instance, plasticity in Ag<sub>2</sub>S has been linked to metallic-like bonding and wavy slip planes<sup>12</sup>, while research on Ag<sub>2</sub>Te<sub>1–x</sub>S<sub>x</sub> solid solutions has uncovered a mechanism involving stress-induced sublattice amorphization stabilized by mobile Ag ions<sup>19,46</sup>. In Ag<sub>2</sub>Te nanowires, plasticity is

attributed to the synergistic effects of dislocation emission, slip band formation, deformation twinning, and Ag nanobridges<sup>47</sup>. This disparity indicates that a one-size-fits-all model is insufficient, and material-specific mechanisms await discovery.

Ag<sub>2</sub>Te is a semiconductor with both ionic and covalent bonding characteristics<sup>48–54</sup> that exhibits remarkable room-temperature plasticity<sup>17,55</sup> and is concurrently recognized as a promising near-room-temperature thermoelectric material<sup>17,50,55–58</sup>. The plasticity enhancement strategies for Ag<sub>2</sub>Te have continuously developed to tackle the inherent brittleness bottleneck of inorganic semiconductors, progressing from nano-structuring (e.g., nanowires)<sup>47</sup> to micro-engineering (e.g., domain boundaries)<sup>55</sup> and down to atomic-scale mechanisms (e.g., sublattice amorphization)<sup>46</sup>. These mechanisms not only significantly improve ductility (achieving strains up to 75.7% in nanowires and tensile ductility of 10,150% in bulk materials) but also optimize thermoelectric performance through phonon scattering (with ZT values enhanced to 0.6–2.2). Intriguingly, while high-S

<sup>1</sup>State Key Laboratory of Advanced Technology for Materials Synthesis and Processing, Wuhan University of Technology, Wuhan, China. <sup>2</sup>Hubei Longzhong Laboratory, Wuhan University of Technology (Xiangyang Demonstration Zone), Xiangyang, Hubei, China. <sup>3</sup>Yangtze Laboratory, Wuhan, China. <sup>4</sup>These authors contributed equally: Anan Guo, Keke Liu. ✉ e-mail: [wujs@whut.edu.cn](mailto:wujs@whut.edu.cn)

materials are generally ductile<sup>59</sup>, Ag<sub>2</sub>Te stands out as one of the ductile high-Te materials, suggesting a potentially unique deformation mechanism. Here, we combine macroscopic tests with in-situ electron microscopy to reveal the origin of plasticity in Ag<sub>2</sub>Te. We discover a previously unrecognized mechanism—ionic-hop-mediated domain rotation—that is distinct from both conventional dislocation slip and the recently reported sublattice amorphization. In this process, the crystalline Te-sublattice undergoes a coordinated large rotation, enabled by the discrete stress-induced hopping of Ag ions. This work not only resolves the deformation mechanism in Ag<sub>2</sub>Te but also establishes a strategy for achieving plasticity in functional semiconductors by harnessing ion migration to drive crystalline reconfiguration, thereby bridging the understanding of its exceptional mechanical and electronic properties.

## Results

### Room-temperature plasticity in Ag<sub>2</sub>Te

Although there are many structural variants, the  $\alpha$ -Ag<sub>2</sub>Te sample used in our experiments is determined to have the monoclinic structure ( $a = 8.1616 \text{ \AA}$ ,  $b = 4.4665 \text{ \AA}$ ,  $c = 8.9733 \text{ \AA}$ ,  $\beta = 124.153^\circ$ ) as indexed by the powder X-ray diffraction (XRD) pattern (Supplementary Fig. 1). Using

the MTS universal test machine (Supplementary Fig. 2a), the tensile ductility of bulk Ag<sub>2</sub>Te at room temperature has been observed. The size of beams being tested is  $8 \times 4 \times 3 \text{ mm}^3$  (Fig. 1a). Figure 1b shows the typical room-temperature stress/strain curve of Ag<sub>2</sub>Te, under the applied tensile stress. Although variations (surface roughness and other factors) during the preparation of Ag<sub>2</sub>Te beams caused discrepancies in the measured results (Supplementary Fig. 2b), the majority of measured results are close to those presented in Fig. 1b. All the samples show a large tensile deformation at room temperature with the average tensile strain of  $\sim 12.13\%$ . Furthermore, optical photos of the Ag<sub>2</sub>Te beam before and after tensile testing (Supplementary Fig. 2c) show a nearly uniform elongation due to the ductile deformation.

We then investigated the tensile properties of Ag<sub>2</sub>Te at a microscopic level by in-situ tensile force S/TEM experiment (Fig. 1c, d and Supplementary Videos 1–3). The schematic of the nanochip used in the tensile force experiments is shown in Supplementary Fig. 3. The Ag<sub>2</sub>Te sample was cut into a beam of  $800 \times 300 \times \sim 100 \text{ nm}^3$  by focused ion beam (FIB) and then the force was applied along the longest edge. As shown in Fig. 1c, before the force was applied, the thin beam is a single crystal oriented along the [021] zone axis, identified by the high-angle

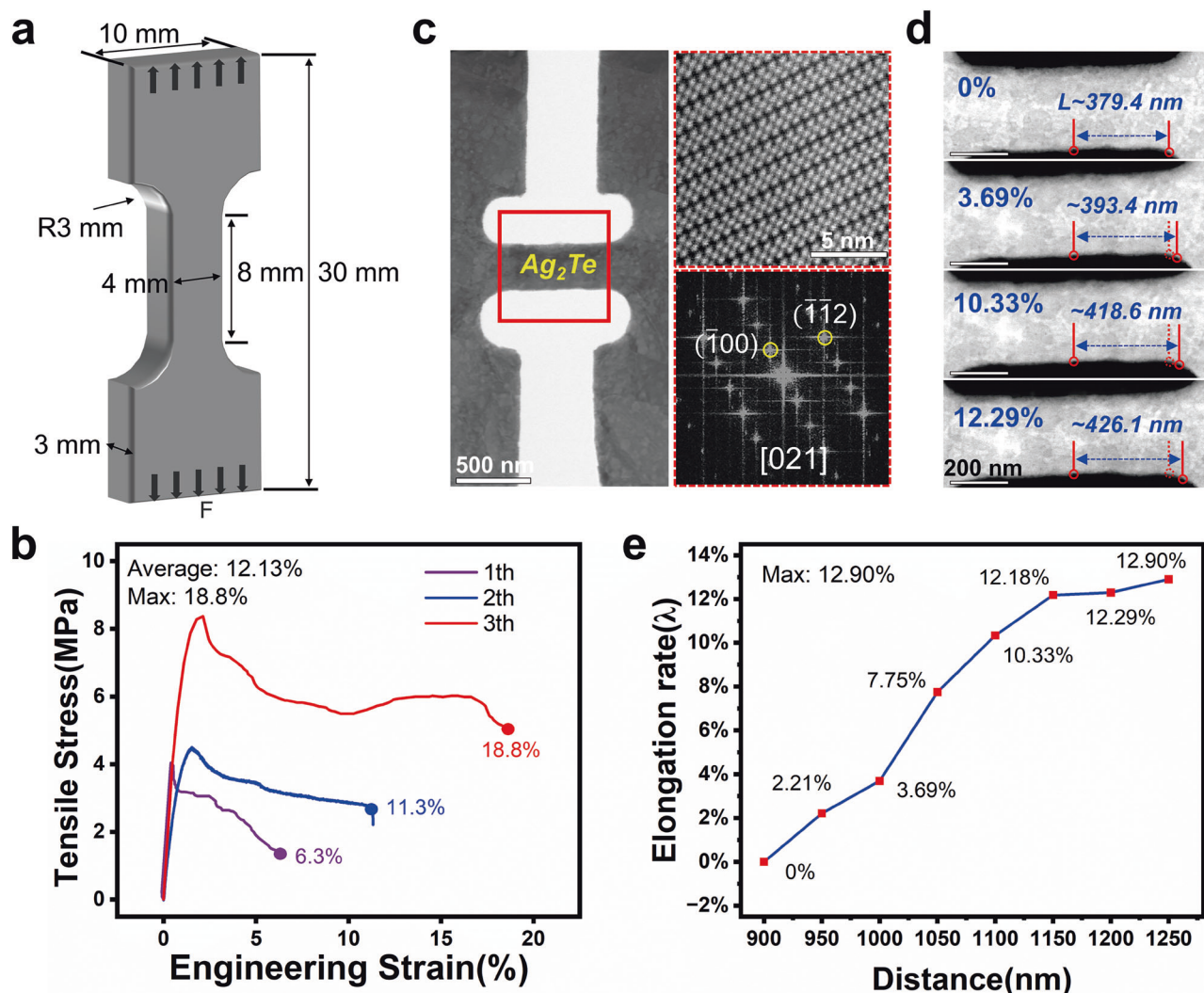


**Fig. 1 | The tensile ductility of Ag<sub>2</sub>Te at room temperature.** **a** The tensile sample size shape. The strain rate for the bulk tensile test was  $0.2 \text{ mm} \cdot \text{s}^{-1}$ . And the tensile direction was along the longest dimension of the dog-bone-shaped sample. This diagram was created using PowerPoint. **b** The tensile stress-strain curve of bulk Ag<sub>2</sub>Te. **c** Low-magnification bright field (BF) image and high-magnification HAADF-

STEM image of the Ag<sub>2</sub>Te tensile beam before deformation, oriented along the [021] zone axis. **d** HAADF-STEM images of the Ag<sub>2</sub>Te beam under tension at strains of 0%, 3.69%, 10.33% and 12.29%. **e** The curve of elongation rate ( $\lambda$ ) during the in-situ tensile force S/TEM experiment.

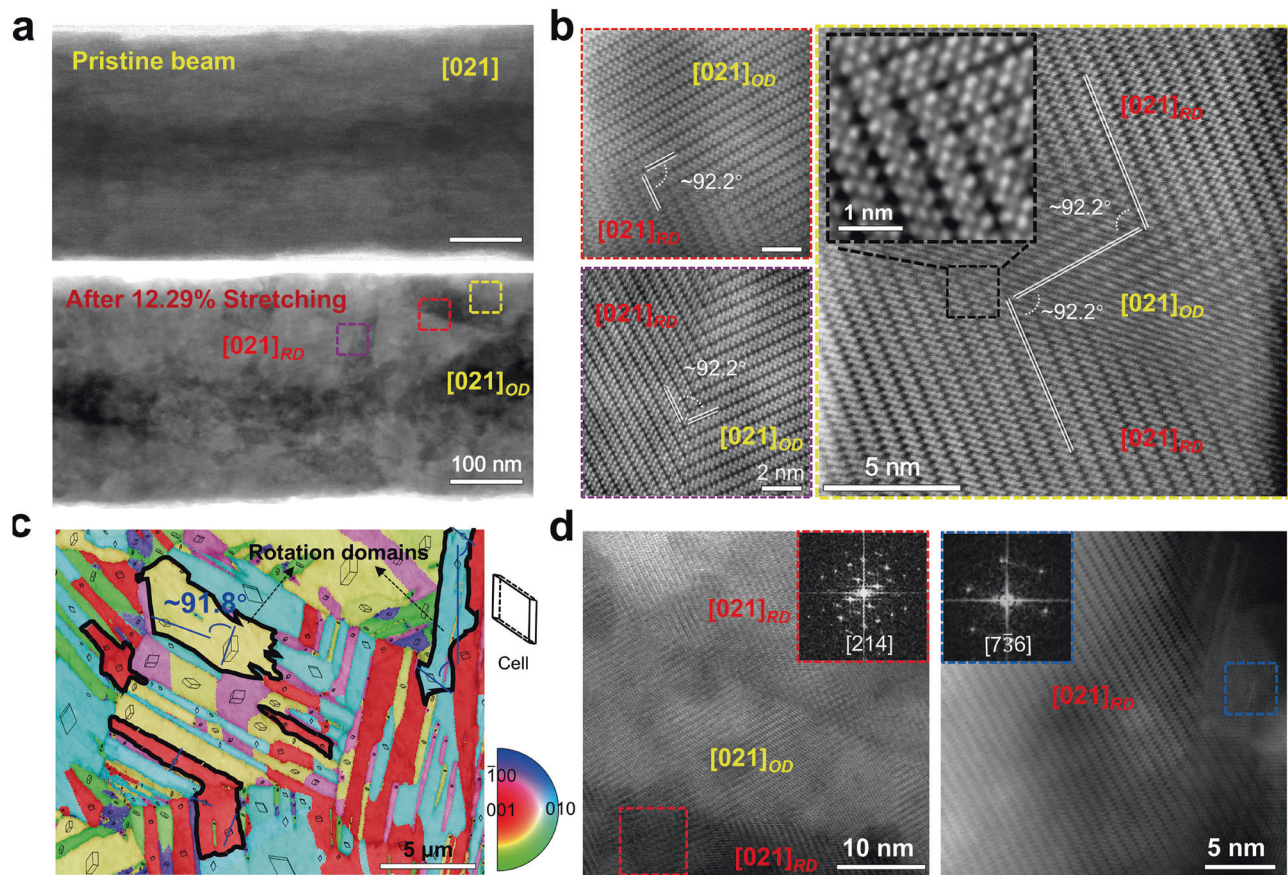


**Fig. 2 | The domain transition in  $\text{Ag}_2\text{Te}$  under stress. a** BF images of the  $\text{Ag}_2\text{Te}$  tensile beam before and after stretching, showing the formation of multiple domains. **b** Atomic-scale HAADF-STEM images of the boundary of the [021]<sub>OD</sub> and [021]<sub>RD</sub> domains marked in **A**. **c** EBSD image of domain structure for the fracture of

the bulk  $\text{Ag}_2\text{Te}$  sample after stretching. **d** HAADF-STEM image of the [021]<sub>RD</sub> domain, with minor domains along other zone axes (e.g., [214], [736]) also observed, indicating the complex stress state during deformation.

annular dark-field scanning transmission electron microscopy (HAADF-STEM) image and the corresponding fast Fourier transform (FFT) image. When the tensile force was applied, the beam was gradually elongated (Supplementary Videos 1–3). Figure 1d shows the HAADF-STEM images of  $\text{Ag}_2\text{Te}$  when the deformation reaches 0%, 3.69%, 10.33% to 12.29%, respectively. The maximum tensile strain of the beam reaches 12.9% before fracture, as shown in Fig. 1e, similar with that observed in bulk  $\text{Ag}_2\text{Te}$ . As shown in Supplementary Fig. 4a, after fracture of the beam, there is no clear sign of necking, and the fractured  $\text{Ag}_2\text{Te}$  has the same crystalline structure, as identified by STEM imaging. Also, the stoichiometric ratio of Ag to Te remains as the 2:1, as identified by the energy dispersive spectrometer (EDS) mapping and the corresponding line-scan quantification (Supplementary Fig. 4b). These observations imply that the  $\text{Ag}_2\text{Te}$  has plasticity at room temperature, while its deformation mechanism may be different from those of plastic metals.

### The microstructural mechanism of room-temperature plasticity

We find that the large tensile deformation of  $\text{Ag}_2\text{Te}$  is primarily mediated by the formation of coherent rotation domains—crystallographic regions that undergo a specific  $-92^\circ$  lattice reorientation relative to the original matrix. Crucially, our analysis reveals that conventional defects like dislocations, twins, or stacking faults are conspicuously absent as dominant features in the deformed microstructure.

The microstructure evolution in  $\text{Ag}_2\text{Te}$  during stretching was investigated. As shown in Fig. 2a, numerous rotation domains formed within the original [021]-oriented  $\text{Ag}_2\text{Te}$  crystal after deformation.

HAADF-STEM imaging (Fig. 2b) clearly identifies both the original [021] domain ([021]<sub>OD</sub>) and a newly formed [021] rotation domain ([021]<sub>RD</sub>). The two domains maintain a coherent boundary and are related by a consistent rotation angle of  $-92.2^\circ$ .

The FFT patterns from the [021]<sub>OD</sub> and [021]<sub>RD</sub> (Supplementary Fig. 5a) provide definitive crystallographic evidence that this is a rotation domain, not a twin. The yellow dashed line in the FFT represents the trace of the (01 $\bar{2}$ ) plane, which would be the mirror plane if this were a deformation twin. This trace is determined geometrically as the line through the FFT center that is perpendicular to the vector connecting the center to the (01 $\bar{2}$ ) diffraction spot. As demonstrated, the diffraction spots from the [021]<sub>RD</sub> (red circles) do not have a mirror symmetry to these spots from the [021]<sub>OD</sub> (blue circles) across this line. Instead, the entire diffraction pattern from the [021]<sub>RD</sub> is rotated by  $-92.2^\circ$  with respect to that of the [021]<sub>OD</sub> (Supplementary Fig. 5b). The absence of such mirror symmetry confirms the non-twinned nature of the domain boundary.

Such a similar domain transition was also observed in the tensile experiment of bulk  $\text{Ag}_2\text{Te}$  as evidenced by the electron backscatter diffraction (EBSD) mapping as shown in Fig. 2c and Supplementary Fig. 6. The EBSD map (Fig. 2c) clearly shows the formation of many rotation domains near the fracture of the bulk sample. The angle between the two rotation domains is close to  $-91.8^\circ$  (as marked by the blue lines in Fig. 2c), similar to the orientation domains observed by in-situ S/TEM (Fig. 2b). In comparison, far fewer rotation domains are observed in the area far from the fracture (Supplementary Fig. 6b). It can be deduced that the rotation domains are formed under tensile stress, especially the areas that underwent a large deformation.

Furthermore, the fracture morphology of bulk  $\text{Ag}_2\text{Te}$  as shown in Supplementary Fig. 6a reveals no evidence of necking, consistent with the observations in both Supplementary Fig. 2c and Supplementary Fig. 4a. This behavior starkly contrasts with the deformation characteristics of most plastic metals. The deformation in  $\text{Ag}_2\text{Te}$  stems from the stress-induced rotational domain transformation. Unlike conventional plastic deformation, which relies on localized shear deformation through dislocation slip, domain transformation represents a continuous nucleation and growth process throughout the material matrix. When external forces are applied, numerous rotational domains sequentially nucleate within stress-concentrated regions, collectively coordinating macroscopic strain. This distributed, non-localized strain coordination effectively prevents the concentration of plastic instability within narrow regions, thereby suppressing necking formation. Consequently, the observation of “neck-free” deformation supports our proposed mechanism where domain transformation dominates and coordinates plastic deformation.

While the major contribution to the deformation is from formation of the rotation domains, the other form of domain transition, i.e., the formation of a small number of domains along other orientations, is also observed. As shown in Fig. 2d, small domains along the [214] and [736] axis are observed. Due to the complex interaction of the applied stress and the polycrystalline sample, it is not surprising that small domains along other zone axis are occasionally found during the stretching deformation.

### Atomic mechanism of room-temperature plasticity

Our atomic-scale observations reveal that the plasticity of  $\text{Ag}_2\text{Te}$  originates from a stress-driven ionic-hop-mediated domain rotation. This process is initiated by an anisotropic deformation of the rigid Te-sublattice, which triggers the coordinated hopping of Ag ions, ultimately leading to a macroscopic crystal reorientation.

As shown in the HAADF-STEM image (Fig. 3a) and the corresponding schematic (Fig. 3b), the transformation under tensile stress

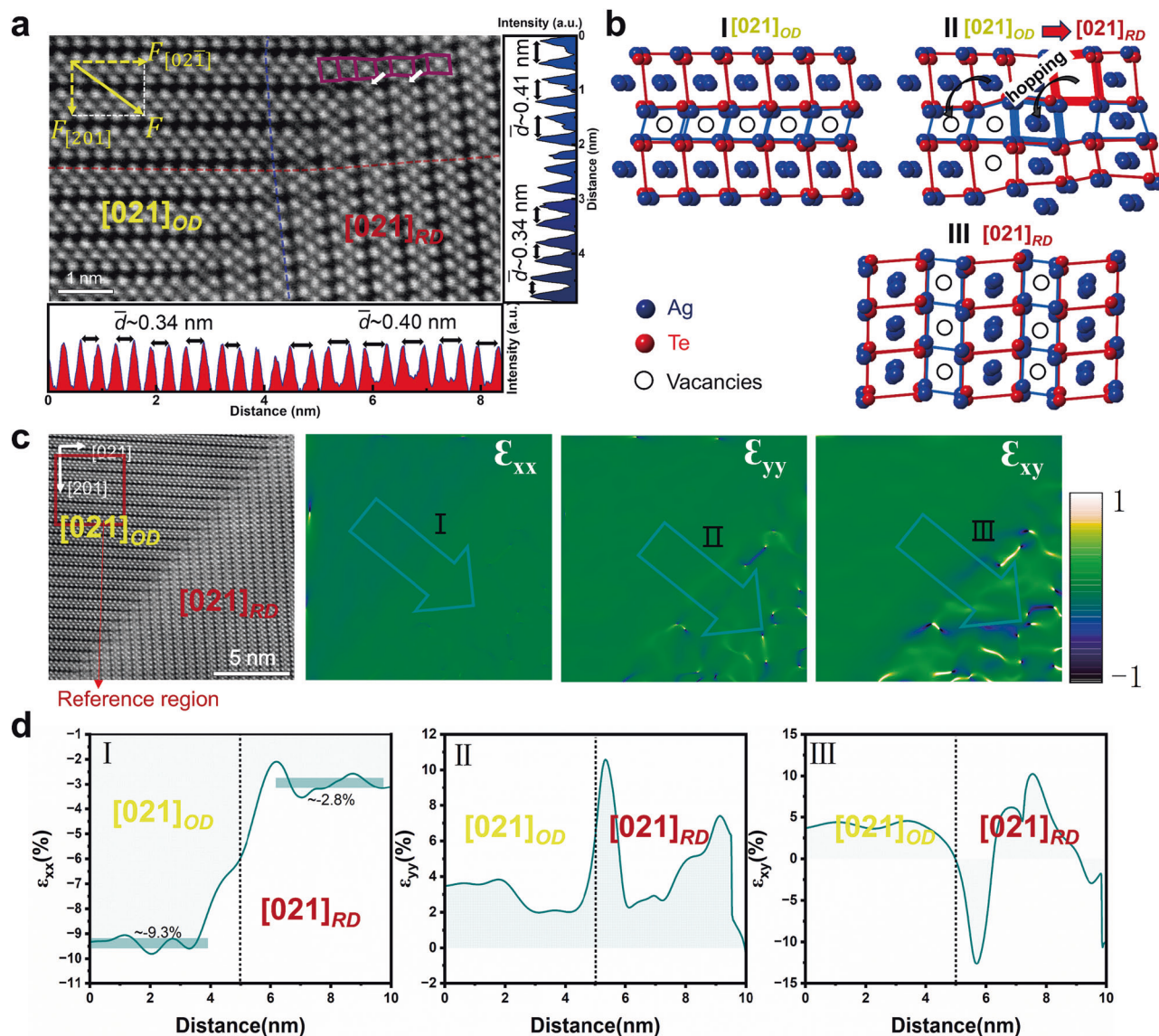


**Fig. 3 | Atomic mechanism of the domain transition in  $\text{Ag}_2\text{Te}$ .** **a** Atomic-scale HAADF-STEM image of the boundary of  $[021]_{OD}$  and  $[021]_{RD}$  domains. The purple rectangles highlight the Te-sublattice in the original domain ( $[021]_{OD}$ ) and the rotation domain ( $[021]_{RD}$ ), illustrating the anisotropic deformation of the Te-sublattice, referring to elongation along the tensile axis ( $F_{[021]}$ ) direction and compression along the transverse direction ( $F_{[201]}$ ) direction. **b** Atomic model diagram

of the domain boundary. **c** Strain maps of the boundary of  $[021]_{OD}$  and  $[021]_{RD}$  domains. The reference region is selected from the unstrained area (top-left corner, as outlined by the red rectangle) of the  $[021]_{OD}$  to ensure computational accuracy. **d** Strain profiles across the domain boundary. Line profiles of the strain components ( $\epsilon_{xx}$ ,  $\epsilon_{yy}$ ,  $\epsilon_{xy}$ ) measured along the path from  $[021]_{OD}$  to  $[021]_{RD}$  in **c**.

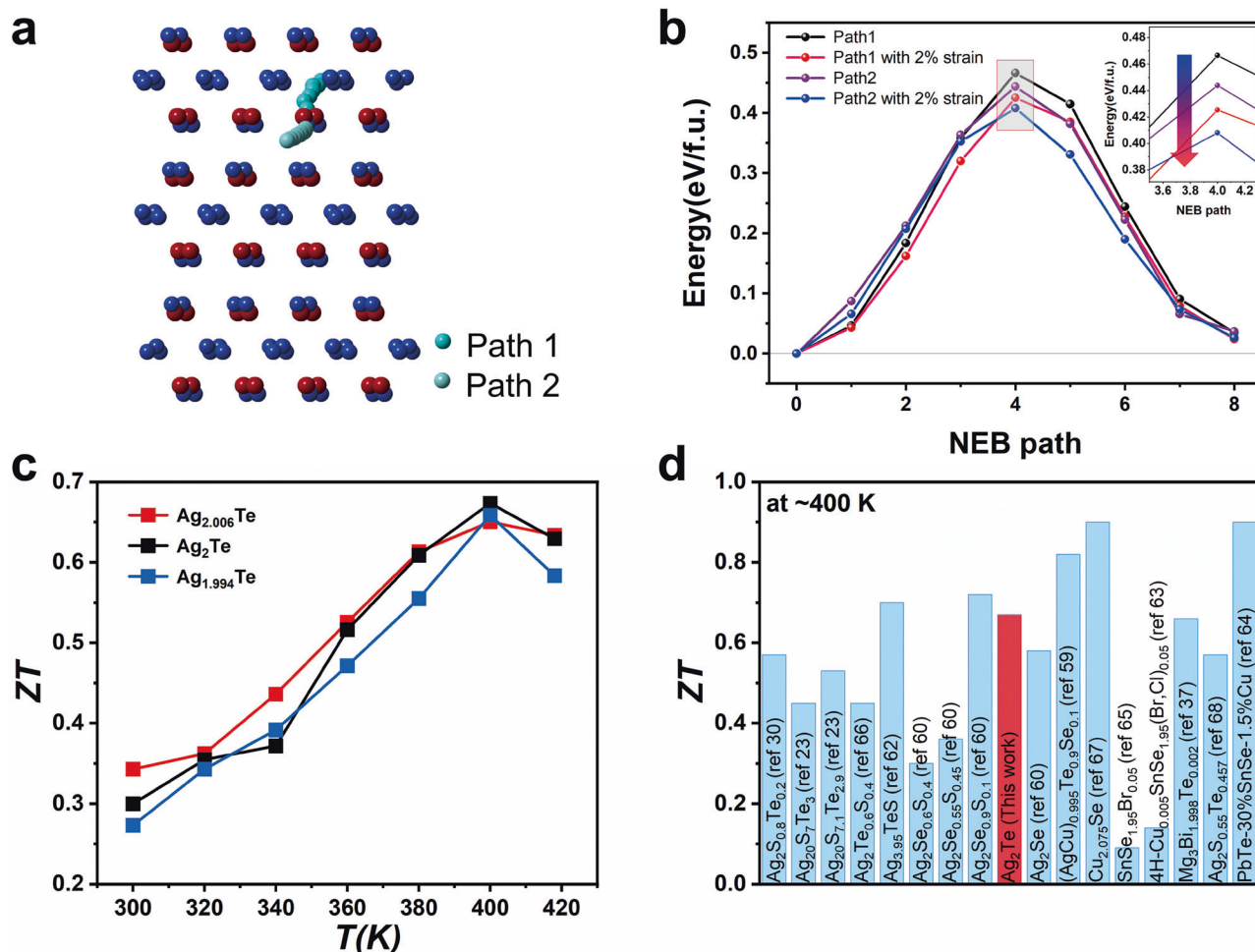


**Fig. 4 | DFT calculation of ions migration and diffusion coefficients in  $\text{Ag}_2\text{Te}$ .** **a** Atomic models showing the two most probable migration paths for Ag ions between adjacent tetrahedral sites. **b** DFT-calculated energy barriers for Ag migration along Path 1 and Path 2 without and with (inset) applied strain, demonstrating the strain-induced reduction of the migration barrier. The 2% tensile strain was applied within the (100) plane, which is the primary shear plane corresponding to the direction of the applied tensile stress in the in-situ TEM experiments. This specific loading condition was chosen to directly mimic the stress state that

activates the ionic-hop-mediated domain rotation observed experimentally. **c** Temperature-dependent ZT of  $\text{Ag}_{2+x}\text{Te}$ . **d** Comparison of the thermoelectric figure of merit (ZT) at a uniform temperature of  $\sim 400$  K for representative room-temperature ductile semiconductors. This comparison highlights the competitive thermoelectric performance of  $\text{Ag}_2\text{Te}$ , which, when integrated with its plasticity mechanism, positions it as a promising model system for flexible electronics. Data sources: refs. 9,23,30,37,59–67.

involves a substantial deformation of the Te-sublattice. The spacing between the atomic columns identified as Te-dominated (specifically, Te-Ag mixed columns) by image simulation (Supplementary Fig. 7) substantially increases from 0.34 nm to 0.40 nm along the tensile axis, while being compressed transversely. This distortion directly squeezes the Ag ions out of their original tetrahedral sites. In the structure of  $\text{Ag}_2\text{Te}$  (Supplementary Fig. 8a), both Ag1 and Ag2 sites reside within Te tetrahedra, with intrinsic vacancies concentrated in the (100) plane (Supplementary Fig. 8b). The stress forces the Ag ions to hop into these adjacent vacant sites within the expanded tetrahedra. This discrete, stress-induced ionic hop is the critical step that unlocks the lattice, allowing the entire vacancy-concentrated (100) plane to undergo a coordinated  $-92.2^\circ$  rotation, thereby forming the new domain.

The resulting strain distribution, mapped by geometric phase analysis (GPA) in Fig. 3c and quantified in Fig. 3d, provides direct evidence of how strain is accommodated under the mechanism. The  $-92.2^\circ$  rotation effectively releases the elastic strain, as seen in the relaxation of the  $\epsilon_{xx}$  component from  $\sim -9.3\%$  in the  $[021]_{OD}$  to  $\sim -2.8\%$  in the  $[021]_{RD}$ . Based on the hopping model, the predicted tensile deformation along the main stress direction is  $-17.6\%$ , which aligns with the maximum strain observed in the bulk tensile tests (Supplementary Fig. 2).

First-principles DFT calculations were performed to quantitatively validate this atomic-scale hopping mechanism. We calculated the migration barriers for the two most probable paths (Path 1 and Path 2, Fig. 4a) connecting adjacent tetrahedral sites involved in the domain rotation. The calculations show that the migration barriers for both paths are comparable, at about 0.47 eV and 0.44 eV without strain (Fig. 4b), indicating low anisotropy for ion hopping, which facilitates cooperative migration. Crucially, under a 2% lattice strain (within the (100) plane), the barrier for path 1 is reduced to 0.43 eV (inset of Fig. 4b), demonstrating that the deformation of the Te-sublattice actively promotes Ag ions migration. Furthermore, the calculated diffusion coefficient of  $\text{Ag}^+$  is  $\sim 25$  times larger than that of  $\text{Te}^{2-}$  (Supplementary Fig. 9b), confirming the preferential mobility of the cations. Together, these calculations confirm that the deformation-induced hopping of Ag ions is a feasible and favorable process. The critical role of  $\text{Ag}^+$  migration suggests that the stoichiometry, and hence the Ag vacancy concentration, in  $\text{Ag}_{2+x}\text{Te}$  is expected to be a key factor in modulating its plastic behavior, offering a promising avenue for future materials engineering.

Both a strain-softening and strain-hardening effects are observed in the macroscopic tensile responses in bulk  $\text{Ag}_2\text{Te}$ , as shown in Fig. 1b and

Supplementary Fig. 2b, respectively. When the tested samples have a different microstructure, the domain rotation mechanism could manifest in different modes. When there forms small number of new domain boundaries in big grains, one may observe the strain-softening effect (as shown in Fig. 1b). When involving the sequential nucleation of multiple domain boundaries, their cumulative interactions can lead to strain-hardening by resisting further deformation (as shown in Supplementary Fig. 2b). Both in-situ and ex-situ microstructural study on the deformed  $\text{Ag}_2\text{Te}$  samples reveal the deformation is mainly accommodated by the formation of rotation domains and domains boundaries. We seldom observe other defects (such as twins, stacking faults and dislocations) in the deformed areas. However, as dislocations refer to the lattice mismatch, in the boundary of  $[021]_{RD}$  and  $[\bar{7}36]$  domains (despite formation of the  $[\bar{7}36]$  domain is rare, Fig. 2d), there would be complicated dislocations to accommodate the lattice mismatch.

In conclusion, we have unveiled a previously unrecognized plasticity mechanism in  $\text{Ag}_2\text{Te}$ : stress-driven ionic-hop-mediated domain rotation. It is the synergistic interplay between the deformation of the Te-sublattice and the subsequent hopping of Ag ions that enables the large, coherent lattice rotation, distinguishing it fundamentally from conventional dislocation-based plasticity or deformation twinning.

### Compatibility of plasticity and thermoelectric properties

The practical potential of a functional semiconductor is determined by the synergy between its mechanical and electronic properties. In  $\text{Ag}_2\text{Te}$ , the room-temperature plasticity governed by ionic-hop-mediated domain rotation is complemented by its decent thermoelectric performance. The conductivity ( $\sigma$ ), Seebeck coefficient ( $\alpha$ ), power factor (PF), and thermal conductivity ( $\kappa$ ) are shown in Supplementary Fig. 10d. The electrical conductivity shows a metallic-like temperature dependence, while the Seebeck coefficient indicates n-type conduction. As shown in Fig. 4c, a peak ZT value of  $-0.67$  is achieved at 400 K. A direct comparison at a uniform temperature of  $-400\text{ K}^{9,23,30,37,60-68}$  (Fig. 4d) confirms that this ZT value is comparable to other state-of-the-art room-temperature ductile semiconductors. This demonstrates that  $\text{Ag}_2\text{Te}$  successfully combines a unique deformation mechanism with high thermoelectric performance, suggesting its potential for flexible thermoelectric applications.

The compatibility of this unique plasticity mechanism with functional properties is a key advantage. Prior studies on closely related  $\text{Ag}_2\text{Te}_{1-x}\text{Se}_x$  compounds have demonstrated that extraordinary room-temperature plastic deformability can coexist with a high thermoelectric Figure of merit ( $\text{ZT} > 0.6$ )<sup>17</sup>. This is because chemical stoichiometry and overall chemical bonding preserve during deformation, avoiding introduction of the detrimental defects that would severely degrade electronic transport.

Our discovered mechanism of ionic-hop-mediated domain rotation further distinguishes itself from other plasticity pathways in  $\text{Ag}_2\text{Te}$ . For instance, in  $\text{Ag}_2\text{Te}$  nanowires, exceptional ductility has been attributed to deformation twinning on the (001) plane, followed by Ag precipitation under extreme stress<sup>47</sup>. In contrast, the plasticity in our bulk  $\text{Ag}_2\text{Te}$  samples is achieved without phase separation or twinning, but through a coherent lattice rotation. This distinction underscores the material-specific nature of plastic deformation and highlights the unique advantage of the mechanism in preserving both crystallinity and chemical stoichiometry, a prerequisite for maintaining optimal thermoelectric function.

### Discussion

This study reveals a previously unrecognized plasticity mechanism in the inorganic semiconductor  $\text{Ag}_2\text{Te}$ : stress-driven ionic-hop-mediated domain rotation. By combining macroscopic tests and in-situ tensile S/TEM, we demonstrate that the applied stress induces a large deformation of the Te-sublattice, which in turn triggers the coordinated hopping of Ag ions into adjacent vacancies. This

discrete ionic migration unlocks a coherent  $-92.2^\circ$  rotation of the crystal lattice, accommodating substantial plastic strain while preserving long-range crystallinity and chemical stoichiometry. The Ag ions hopping, quantitatively validated by DFT calculations showing a strain-reduced migration barrier, is the linchpin of this process. It enables a continuous structural adaptation under stress, leading to the room-temperature plasticity (e.g.,  $>10\%$  tensile strain) observed in bulk  $\text{Ag}_2\text{Te}$ . Crucially, this unique deformation mechanism does not preclude functional properties, as evidenced by the material's decent thermoelectric performance ( $\text{ZT} \approx 0.67$  at 400 K). Our work resolves the atomic-scale origin of plasticity in  $\text{Ag}_2\text{Te}$  and establishes ionic-hop-mediated domain rotation as a paradigm for designing flexible functional semiconductors, where mechanical robustness is integrated with electronic functionality through stress-driven ionic reconfiguration.

## Methods

### Materials synthesis

$\text{Ag}_2\text{Te}$  was prepared by vacuum melting and annealing. A stoichiometric amount of Ag (99.99%, Sinopharm, China) strips and Te (99.99%) were weighed and mixed. The mixtures were sealed in evacuated quartz tubes and heated in a furnace, up to  $1273\text{ K}$  at  $1.5\text{ K min}^{-1}$  and kept for 10 h. To obtain homogeneous ingots, the quartz tubes were rocked every 2 h at  $1273\text{ K}$ . Subsequently, the tubes were slowly cooled down to  $673\text{ K}$  at the rate of  $1\text{ K min}^{-1}$ . The resulting ingots were further annealed at  $673\text{ K}$  for 3 days and then cooled down to  $373\text{ K}$ , and held for 2 days. The obtained ingots were cut into a proper shape for characterization and performance measurement. The constituent phases were identified by XRD (Empyrean, Cu  $K_\alpha$  line, PANalytical, Holland) and the result shows that the  $\text{Ag}_2\text{Te}$  in our work has a monoclinic structure, with  $a = 8.1616\text{ \AA}$ ,  $b = 4.4665\text{ \AA}$ ,  $c = 8.9733\text{ \AA}$ ,  $\beta = 124.153^\circ$ ; space group  $P2_1/c$  (Supplementary Fig. 1). Here, we refer to the monoclinic phase as  $\alpha\text{-Ag}_2\text{Te}$ .

### Instrumentation

The tensile tests were performed using an MTS universal testing machine (MTS E44.104, Supplementary Fig. 2a). Key parameters, including the strain rate, elastic modulus, and total strain at fracture, were determined from the tensile stress-strain curves. These parameters reflect the material's plasticity and resistance to elastic deformation. The tensile yield strength, defined as the maximum stress during the failure process, was calculated using the formula:  $\sigma_y = F/(b \times W)$ , where  $F$  represented the maximum applied load,  $b$  was the sample beam thickness, and  $W$  was the sample beam width.

Thin TEM samples were prepared by Focused Ion Beam (FIB) milling (Helios Nanolab G3 UC, FEI). TEM characterization of the samples was carried out using a double Cs-corrected Scanning Transmission Electron Microscope (STEM, Titan Themis G2 60-300, FEI). For the in-situ mechanical experiments, a nanochip with force and thermal holder (Mini-lab, Bestron) was used, as shown in Supplementary Fig. 3b. The TEM sample was machined into the shape of a beam and the force is applied along the longest side of the beam.

### DFT calculation

All structural optimizations were performed using the Vienna Ab initio Simulation Package (VASP) software<sup>69-71</sup>. The Projector Augmented Wave (PAW) method<sup>70,72</sup> and the Perdew-Burke-Ernzerhof (PBE)<sup>71</sup> generalized gradient approximation (GGA) exchange-correlation functional were employed for relaxation calculations. The plane-wave kinetic energy cutoff was set to  $500\text{ eV}$ . A k-point mesh of  $3 \times 6 \times 3$  was used to ensure convergence. By balancing computational cost and accuracy, the total energy convergence criterion for structural optimization was set to  $10^{-8}\text{ eV}$ , and all structures were fully relaxed until the forces acting on all atoms converged to below  $0.01\text{ eV/\AA}$ . Subsequent transition state calculations utilized the climbing image

nudged elastic band (CI-NEB) method<sup>73</sup>, inserting seven images between the initial and final states. Ab initio molecular dynamics (AIMD) simulations were conducted using a  $2 \times 2 \times 4$  supercell containing 192 atoms. The system was simulated in the canonical (NVT) ensemble at 600 K and 773 K, employing a time step of 2 fs for a total simulation time of 8 ps.

The specific Ag migration paths investigated by the CI-NEB method (Fig. 4a) were selected to directly test the atomic-scale mechanism obtained from the experimental observations (Fig. 3b). The initial and final states were defined as the configurations with the Ag ions residing in two adjacent, symmetry-equivalent tetrahedral sites that share a common vacancy. The calculated paths (Path 1 and Path 2) correspond to the most geometrically straightforward hopping trajectories between these sites, which are integral to the domain rotation process.

## Data availability

All data are available in the main Article and Supplementary Information, or from the corresponding author upon a request. Source data are provided with this paper. All data are available in the main text or the supplementary materials. Source data are provided with this paper.

## References

- Chen, H. et al. Room-temperature plastic inorganic semiconductors for flexible and deformable electronics. *InfoMat* **3**, 22–35 (2021).
- Hou, S. et al. Encapsulated Ag<sub>2</sub>Se-based flexible thermoelectric generator with remarkable performance. *Mater. Today Phys.* **38**, 101276 (2023).
- Hwang, H. & Jang, K.-S. Thermoelectric all-carbon heterostructures for a flexible thermoelectric generator. *Sustain. Energy Fuels* **5**, 267–273 (2021).
- Tsai, M.-F. et al. Oxide heteroepitaxy-based flexible ferroelectric transistor. *ACS Appl. Mater. Interfaces* **11**, 25882–25890 (2019).
- Wang, Y. et al. Flexible thermoelectric materials and generators: challenges and innovations. *Adv. Mater.* **31**, 1807916 (2019).
- Wei, T. et al. A graphene-nanoribbon-based thermoelectric generator. *Carbon* **210**, 118053 (2023).
- Zou, Q. et al. Bi<sub>2</sub>Te<sub>3</sub>-based flexible thermoelectric generator for wearable electronics. *Appl. Phys. Lett.* **120**, 023903 (2022).
- Chen, K. et al. Flexible thermoelectrics based on plastic inorganic semiconductors. *Adv. Mater. Technol.* **8**, 2300189 (2023).
- Qiu, P., Deng, T., Chen, L. & Shi, X. Plastic inorganic thermoelectric materials. *Joule* **8**, 622–634 (2024).
- Gao, Z. et al. p-type plastic inorganic thermoelectric materials. *Adv. Energy Mater.* **11**, 2100883 (2021).
- Li, A. et al. High performance magnesium-based plastic semiconductors for flexible thermoelectrics. *Nat. Commun.* **15**, 5108 (2024).
- Shi, X. et al. Room-temperature ductile inorganic semiconductor. *Nat. Mater.* **17**, 421–426 (2018).
- Wu, J. et al. Polymer-like inorganic double helical van der Waals semiconductor. *Nano Lett.* **22**, 9054–9061 (2022).
- Yang, Q. et al. Flexible thermoelectrics based on ductile semiconductors. *Science* **377**, 854–858 (2022).
- Kumar, S., Battabyal, M. & Satapathy, D. K. Flexible Ag<sub>2</sub>Se film with enhanced thermoelectric performance. *ACS Appl. Mater. Interfaces* **16**, 66170–66180 (2024).
- Sun, Y. et al. Van der Waals semiconductor InSe plastifies by martensitic transformation. *Sci. Adv.* **10**, eado9593 (2024).
- Feng, L. et al. Highly deformable Ag<sub>2</sub>Te<sub>1-x</sub>Se<sub>x</sub>-based thermoelectric compounds. *Mater. Today Phys.* **33**, 101051 (2023).
- Gao, Z. et al. High-throughput screening of 2D van der Waals crystals with plastic deformability. *Nat. Commun.* **13**, 7491 (2022).
- Hu, H., Wang, Y., Fu, C., Zhao, X. & Zhu, T. Achieving metal-like malleability and ductility in Ag<sub>2</sub>Te<sub>1-x</sub>S<sub>x</sub> inorganic thermoelectric semiconductors with high mobility. *Innovation* **3**, 100341 (2022).
- Oshima, Y., Nakamura, A. & Matsunaga, K. Extraordinary plasticity of an inorganic semiconductor in darkness. *Science* **360**, 772–774 (2018).
- Wang, Y., Li, A., Hu, H., Fu, C. & Zhu, T. Reversible room temperature brittle-plastic transition in Ag<sub>2</sub>Te<sub>0.6</sub>S<sub>0.4</sub> inorganic thermoelectric semiconductor. *Adv. Funct. Mater.* **33**, 2300189 (2023).
- Wei, T.-R. et al. Exceptional plasticity in the bulk single-crystalline van der Waals semiconductor InSe. *Science* **369**, 542–545 (2020).
- Yang, S. et al. Ductile Ag<sub>20</sub>S<sub>7</sub>Te<sub>3</sub> with excellent shape-conformability and high thermoelectric performance. *Adv. Mater.* **33**, 2007681 (2021).
- Zhang, J. et al. Plastic deformation in silicon nitride ceramics via bond switching at coherent interfaces. *Science* **378**, 371–376 (2022).
- Hou, C. & Zhu, M. Semiconductors flex thermoelectric power. *Science* **377**, 815–816 (2022).
- Mixed Mode Cracking in Layered Materials. in *Advances in Applied Mechanics* 63–191. [https://doi.org/10.1016/s0065-2156\(08\)70164-9](https://doi.org/10.1016/s0065-2156(08)70164-9) (Elsevier, 1991).
- Qiu, J. et al. 3D Printing of highly textured bulk thermoelectric materials: mechanically robust BiSbTe alloys with superior performance. *Energy Environ. Sci.* **12**, 3106–3117 (2019).
- Zhu, Y. et al. Mediating point defects endows n-Type Bi<sub>2</sub>Te<sub>3</sub> with high thermoelectric performance and superior mechanical robustness for power generation application. *Small* **18**, 2201352 (2022).
- Jo, S. et al. Solution-processed stretchable Ag<sub>2</sub>S semiconductor thin films for wearable self-powered nonvolatile memory. *Adv. Mater.* **33**, 2100066 (2021).
- Liang, J. et al. Flexible thermoelectrics: from silver chalcogenides to full-inorganic devices. *Energy Environ. Sci.* **12**, 2983–2990 (2019).
- Zhu, Y., Liang, J., Shi, X. & Zhang, Z. Full-inorganic flexible Ag<sub>2</sub>S memristor with interface resistance-switching for energy-efficient computing. *ACS Appl. Mater. Interfaces* **14**, 43482–43489 (2022).
- Hu, M. et al. Helical dislocation-driven plasticity and flexible high-performance thermoelectric generator in α-Mg<sub>3</sub>Bi<sub>2</sub> single crystals. *Nat. Commun.* **16**, 128 (2025).
- Li, X., Chen, F. & Lu, Y. Ductile inorganic semiconductors for deformable electronics. *Interdiscip. Mater.* **3**, 835–846 (2024).
- Li, X. et al. Multislip-enabled morphing of all-inorganic perovskites. *Nat. Mater.* **22**, 1175–1181 (2023).
- Wu, J. et al. Uncovering the phonon spectra and lattice dynamics of plastically deformable InSe van der Waals crystals. *Nat. Commun.* **15**, 6248 (2024).
- Lu, Y. et al. Staggered-layer-boosted flexible Bi<sub>2</sub>Te<sub>3</sub> films with high thermoelectric performance. *Nat. Nanotechnol.* **18**, 1281–1288 (2023).
- Zhao, P. et al. Plasticity in single-crystalline Mg<sub>3</sub>Bi<sub>2</sub> thermoelectric material. *Nature* **631**, 777–782 (2024).
- Deng, T. et al. Room-temperature exceptional plasticity in defective Bi<sub>2</sub>Te<sub>3</sub>-based bulk thermoelectric crystals. *Science* **386**, 1112–1117 (2024).
- Su, R. et al. Deformation mechanisms in FCC Co dominated by high-density stacking faults. *Mater. Sci. Eng.: A* **736**, 12–21 (2018).
- Chu, C., Guo, Q., Guan, Y., Qiao, Z. & Liu, Y. Deformation mechanisms of a γ' phase strengthened CoNi-based superalloy at high temperatures. *Mater. Sci. Eng. A* **833**, 142587 (2022).
- Ispánovity, P. D. et al. Dislocation avalanches are like earthquakes on the micron scale. *Nat. Commun.* **13**, 1975 (2022).
- Turlo, V. Dislocations as a tool for nanostructuring advanced materials. *Physchem* **1**, 225–231 (2021).

43. Liu, S. et al. High-density deformation nanotwin induced significant improvement in the plasticity of polycrystalline  $\gamma$ -TiAl-based intermetallic alloys. *Nanoscale* **10**, 11365–11374 (2018).
44. Liu, X. et al. Mechanisms of WC plastic deformation in cemented carbide. *Mater. Des.* **150**, 154–164 (2018).
45. Chu, S. et al. In situ atomic-scale observation of dislocation climb and grain boundary evolution in nanostructured metal. *Nat. Commun.* **13**, 4151 (2022).
46. Wang, Y. et al. Iterative sublattice amorphization facilitates exceptional processability in inorganic semiconductors. *Nat. Mater.* **24**, 1545–1553 (2025).
47. Wu, L. et al. Ultrahigh tensile ductility of  $\text{Ag}_2\text{Te}$  nanowire at room temperature. *Adv. Funct. Mater.* **35**, 2423014 (2025).
48. Hamilton, M. A., Barnes, A. C., Howells, W. S. & Fischer, H. E.  $\text{Ag}^+$  dynamics in the superionic and liquid phases of  $\text{Ag}_2\text{Se}$  and  $\text{Ag}_2\text{Te}$  by coherent quasi-elastic neutron scattering. *J. Phys. Condens. Matter* **13**, 2425–2436 (2001).
49. Dalven, R. & Gill, R. Energy gap in  $\beta$ - $\text{Ag}_2\text{Te}$ . *Phys. Rev.* **143**, 666–670 (1966).
50. Fujikane, M., Kurosaki, K., Muta, H. & Yamanaka, S. Thermoelectric properties of  $\alpha$ - and  $\beta$ - $\text{Ag}_2\text{Te}$ . *J. Alloy. Compd.* **393**, 299–301 (2005).
51. Kashida, S. Electronic structure of  $\text{Ag}_2\text{Te}$ , band calculation and photoelectron spectroscopy. *Solid State Ion.* **148**, 193–201 (2002).
52. Usuki, T., Abe, K., Uemura, O. & Kameda, Y. Ionic Conduction in Liquid  $\text{Ag-Se}$  and  $\text{Ag-Te}$  Systems. *J. Phys. Soc. Jpn.* **70**, 2061–2067 (2001).
53. Rom, I. & Sitte, W. Composition dependence of chemical diffusion coefficient and ionic conductivity of  $\alpha'$ - and  $\alpha$ - $\text{Ag}_2\text{Te}$ . *Solid State Ion.* **70–71**, 147–152 (1994).
54. Bürgermeister, A. & Sitte, W. Chemical diffusion in  $\beta$ - $\text{Ag}_2\text{Te}$ . *Solid State Ion.* **141–142**, 331–334 (2001).
55. Wang, H. et al. Synergetic enhancement of strength–ductility and thermoelectric properties of  $\text{Ag}_2\text{Te}$  by domain boundaries. *Adv. Mater.* **35**, e2302969 (2023).
56. Chang, Y. et al. Facile synthesis of  $\text{Ag}_2\text{Te}$  nanowires and thermoelectric properties of  $\text{Ag}_2\text{Te}$  polycrystals sintered by spark plasma sintering. *CrystEngComm* **21**, 1718–1727 (2019).
57. Hu, H. et al. Fast synthesis and improved electrical stability in n-type  $\text{Ag}_2\text{Te}$  thermoelectric materials. *J. Mater. Sci. Technol.* **91**, 241–250 (2021).
58. Zhu, T. et al. Realizing high thermoelectric performance in Sb-doped  $\text{Ag}_2\text{Te}$  compounds with a low-temperature monoclinic structure. *ACS Appl. Mater. Interfaces* **12**, 39425–39433 (2020).
59. Liang, J. et al. Modulation of the morphotropic phase boundary for high-performance ductile thermoelectric materials. *Nat. Commun.* **14**, 8442 (2023).
60. Jiang, J. et al. Achieving high room-temperature thermoelectric performance in cubic  $\text{AgCuTe}$ . *J. Mater. Chem. A* **8**, 4790–4799 (2020).
61. Liang, J. et al. Crystalline structure-dependent mechanical and thermoelectric performance in  $\text{Ag}_2\text{Se}_{1-x}\text{S}_x$  system. *Research* **2020**, 2020/6591981 (2020).
62. Liang, X. & Chen, C. Ductile inorganic amorphous/crystalline composite  $\text{Ag}_4\text{TeS}$  with phonon-glass electron-crystal transport behavior and excellent stability of high thermoelectric performance on plastic deformation. *Acta Materialia* **218**, 117231 (2021).
63. Deng, T. et al. High thermoelectric power factors in plastic/ductile bulk  $\text{SnSe}_2$ -based crystals. *Adv. Mater.* **36**, 2304219 (2024).
64. Xiao, Y. et al. High-ranged ZT value promotes thermoelectric cooling and power generation in n-type  $\text{PbTe}$ . *Adv. Energy Mater.* **12**, 2200204 (2022).
65. Deng, T. et al. Plastic/Ductile Bulk 2D van der Waals Single-Crystalline  $\text{SnSe}_2$  for Flexible Thermoelectrics. *Adv. Sci.* **9**, 2203436 (2022).
66. He, S. et al. Semiconductor glass with superior flexibility and high room temperature thermoelectric performance. *Sci. Adv.* **6**, eaaz8423 (2020).
67. Tak, J.-Y. et al. Ultralow lattice thermal conductivity and significantly enhanced near-room-temperature thermoelectric figure of merit in  $\alpha$ - $\text{Cu}_2\text{Se}$  through suppressed Cu vacancy formation by overstoichiometric Cu addition. *Chem. Mater.* **30**, 3276–3284 (2018).
68. Li, Z. et al. Flexible  $\text{Ag-S-Te}$  System with Promising Room-Temperature Thermoelectric Performance. *ACS Appl. Mater. Interfaces* **15**, 33605–33611 (2023).
69. Kresse, G. & Hafner, J. Ab initio molecular dynamics for liquid metals. *Phys. Rev. B* **47**, 558–561 (1993).
70. Kresse, G. & Joubert, D. From ultrasoft pseudopotentials to the projector augmented-wave method. *Phys. Rev. B* **59**, 1758–1775 (1999).
71. Blöchl, P. E. Projector augmented-wave method. *Phys. Rev. B* **50**, 17953–17979 (1994).
72. Perdew, J. P., Burke, K. & Ernzerhof, M. Generalized gradient approximation made simple. *Phys. Rev. Lett.* **77**, 3865–3868 (1996).
73. Henkelman, G., Uberuaga, B. P. & Jónsson, H. A climbing image nudged elastic band method for finding saddle points and minimum energy paths. *J. Chem. Phys.* **113**, 9901–9904 (2000).

## Acknowledgements

This work was supported by the National Key R&D Program of China (2024YFE0209300) and the National Natural Science Foundation of China (52573254, 52150710537).

## Author contributions

J.W. designed the experiments. K.L. did the DFT calculation under the guidance of X.S. (Xianli Su). L.L. and L.Y. performed material syntheses under the guidance of X.S. (Xianli Su), D.Y. and X.T. Y.L. done the EBSD test and analyses under the guidance of X.S. (Xiahan Sang). A.G. performed microstructure characterizations, and sample measurements and prepared the samples for in-situ TEM and STEM and performed the in-situ mechanics and electrical experiments under the guidance of J.W., and the help of Q.Z. and Z.W. A.G. collected the data, provided explanations under the guidance of J.W. and wrote the manuscript. J.W. revised the manuscript. All authors contributed helpful discussions to this work.

## Competing interests

The authors declare no competing interests.

## Additional information

**Supplementary information** The online version contains supplementary material available at <https://doi.org/10.1038/s41467-026-69298-z>.

**Correspondence** and requests for materials should be addressed to Jinsong Wu.

**Peer review information** *Nature Communications* thanks the anonymous reviewer(s) for their contribution to the peer review of this work. A peer review file is available.

**Reprints and permissions information** is available at <http://www.nature.com/reprints>

**Publisher's note** Springer Nature remains neutral with regard to jurisdictional claims in published maps and institutional affiliations.

**Open Access** This article is licensed under a Creative Commons Attribution-NonCommercial-NoDerivatives 4.0 International License, which permits any non-commercial use, sharing, distribution and reproduction in any medium or format, as long as you give appropriate credit to the original author(s) and the source, provide a link to the Creative Commons licence, and indicate if you modified the licensed material. You do not have permission under this licence to share adapted material derived from this article or parts of it. The images or other third party material in this article are included in the article's Creative Commons licence, unless indicated otherwise in a credit line to the material. If material is not included in the article's Creative Commons licence and your intended use is not permitted by statutory regulation or exceeds the permitted use, you will need to obtain permission directly from the copyright holder. To view a copy of this licence, visit <http://creativecommons.org/licenses/by-nc-nd/4.0/>.

© The Author(s) 2026